J. Fluid Mech. (1976), *vol.* 78, *part* 2, *pp.* 317–335
Printed in Great Britain

Experiments on a viscous fluid flow between concentric rotating spheres

By MANFRED WIMMER
Institut für Strömungslehre und Strömungsmaschinen,
Universität Karlsruhe, Germany

(Received 23 October 1975)

Some experimental results on incompressible viscous fluid flow in the gap between two concentric rotating spheres are discussed. The flow field in the spherical gap has been studied qualitatively by flow visualization (photographs) and quantitatively by measurements by the hot-wire technique. For a wide range of Reynolds numbers, the friction torque was measured for several gap widths and a relatively simple method of determining the torque theoretically is given. At higher Reynolds numbers instabilities appear. Their different behaviour for relatively small and large gap widths is demonstrated. For the larger gap widths, the different appearance of the Taylor–Görtler vortices, the reason for their generation, their regimes of existence as well as their influence on the friction torque are thoroughly treated. Detailed information is given on the new effect of the dependence of the wavelength of the vortices on the Reynolds number.

1. Introduction

Flow of a viscous fluid between concentric rotating spheres has been the subject of growing interest in recent years, but most of the publications are limited to theoretical treatment of the problem. Among others, there are the papers by Bratukhin (1961), Ovseenko (1963), Yakushin (1968, 1969, 1970), Brailovskaya, Astafeva & Yavorskaya (1972) and Munson & Joseph (1970) as well as Ritter (1973). On the other hand, experimental treatises are sparse. There is one by Khlebutin (1968), one by Sawatzki & Zierep (1970), one by Zierep & Sawatzki (1970) and a recent one by Munson & Menguturk (1975). The papers by Khlebutin (1968) and Sawatzki & Zierep (1970) deal with results for narrow and medium-sized (in their terminology, large) gaps. In the current paper, the gap sizes are of the same order of magnitude. Munson & Menguturk (1975) discussed besides medium-sized gaps (in their terminology narrow) a wide and a very wide gap. Therefore some misunderstandings over the description of the gap size might arise, but all authors give quantitative data for the gap geometry, so that no errors are possible concerning their results.

All the authors write in the experimental part of their papers mainly about instabilities and related friction-torque measurements. The present paper is part of an extensive experimental study of the problem (Wimmer 1974) and tries to reconcile the new effects found here with those known already, and to give a survey of the whole subject.

The entire problem is closely related to the flow between cylinders, but there are some significant differences. Because of the rotation of the spheres, one obtains a three-dimensional basic flow field. For that reason, the flow between rotating spheres is an extension of the well-known contribution of Taylor (1923), who studied the motion in the gap between two coaxial rotating cylinders. In all the investigations described by Taylor (1923), Coles (1965), Donnelly (1965) and others, the basic flow is only one-dimensional, i.e. a circular Couette flow, whereas the basic flow between rotating spheres is fully three-dimensional. There are other differences between the two types of flow. For spheres, the centrifugal forces are a function of the latitude, and because the centrifugal forces are responsible for the instabilities, different types of flow, stable and unstable, exist side by side. Another advantage is that there are no unpleasant boundary effects like those caused in the cylindrical case by the end plates. That is why conditions postulated by the theory can be fulfilled nearly ideally in the case of rotating spheres.

2. Possible configurations and apparatus

Many configurations are possible for rotating spheres. The radius and the angular-velocity ratios of the spheres may be varied. Figure 1 shows the several possibilities. The arrangement in the middle is the general case. Both radii are finite and both spheres are rotating, in the same or in opposite directions. In case 2, only the inner sphere is rotating, the outer one being stationary. If the outer radius tends to infinity, one obtains case 1: a free rotating sphere in an infinite medium. Likewise, if the inner radius tends to zero we obtain case 4: a rotating spherical container filled with a liquid. The two limiting cases are included as well because, as was proved by making comparisons with many appropriate experiments, the small region near the equator may be considered as a region between two rotating cylinders, approximately, and the vicinity of the pole as that above or below a rotating disk in a housing (cf. § 5 and figure 14*d*, plate 4). The present paper deals with case 2 only, i.e. the inner sphere is rotating and the outer one is at rest. For more details concerning case 1, a free rotating sphere in an infinite medium, see Sawatzki (1970). Cases 3, 4 and 5 will be discussed in later publications.

The problems associated with different configurations or with different experimental conditions for the same configuration, such as no vibrations, low friction in the apparatus, flow visualization, hot-wire measurements (oil, air and helium) etc., can not be studied with a single set of apparatus. That is why several test arrangements were set up which met the special conditions. Figure 2 shows a sketch of the arrangement for the friction-torque measurements. It is the experimental set-up which was constructed first and had already been used by Sawatzki & Zierep (1970), but here the axis of rotation is horizontal, contrary to all other experimental set-ups. All the different experimental set-ups are, however, basically the same. There is a rotating inner sphere made of aluminium (11) and a transparent Plexiglas spherical outer shell (12) of 80 mm radius, which is kept constant for all experiments. The radius of the inner sphere is varied. In this way one obtains gap widths $s \equiv R_2 - R_1$ of 0·5–30 mm and corresponding relative

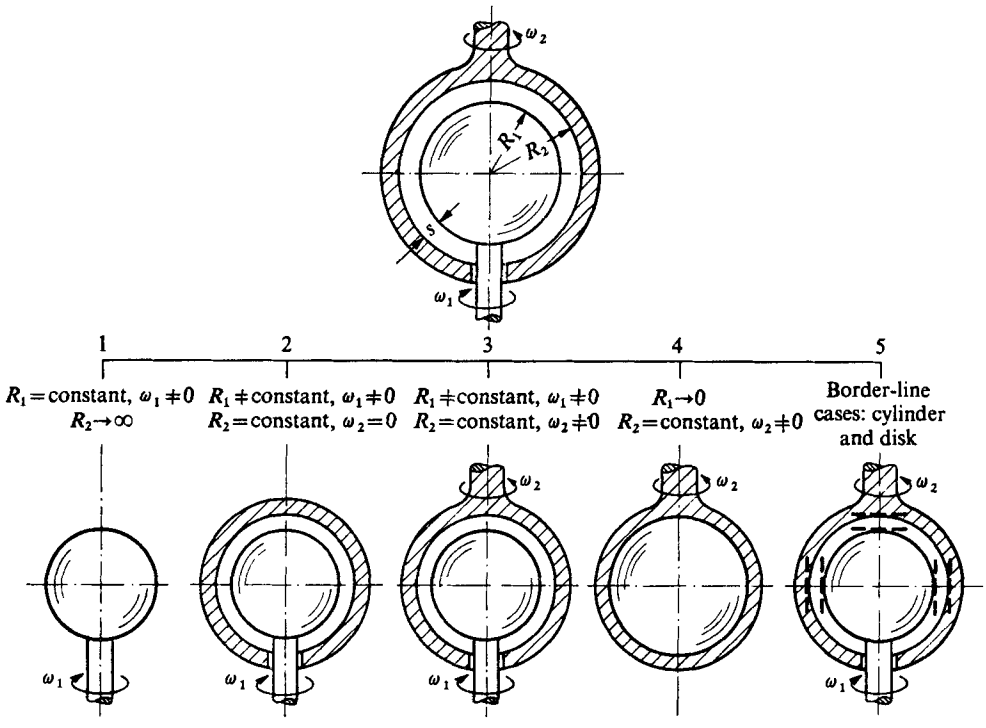

FIGURE 1. Possible configurations.

gap widths $\sigma \equiv s/R_1 = 0{\cdot}0063$–$0{\cdot}60$. The inner sphere, and later the outer one, is driven by a variable-speed electric motor (6). To measure friction torque, the motor is installed as a pendulum (3). The torque is determined by an attached lever (4) and a set of weights (5). The speed of rotation is controlled without friction by using a stroboscope (7) or photo-optics. The temperature is measured in order to determine the viscosity of the fluid in the annulus by thermocouples or thermistors (10). Air and silicone oils (available at Fa. Bayer, Leverkusen, trade name M 3 to M 1000) of various viscosities, $\nu = 1$–1000 cS, were used as the fluid. In this way, and by varying the speed of rotation, a range of Reynolds numbers from $Re = 10^2$ to 10^6 can be covered.

For the flow visualization, a small amount of aluminium flakes (typical mean dimension is 50 μm and a concentration of about 2 g/dm^3 produces good signals) is suspended in the fluid; this amount is small enough not to influence the viscosity or the flow field. For some purposes, like making separate regions of flow or the flow development visible, it is better to employ dye injection. Using this technique, it is important to inject only a small amount of very concentrated dye in order not to disturb the flow field to be observed. Also it is important that the injected dye has the same temperature and density as the fluid in the annulus. The best dye used during these experiments was Ceresblau GN (available at Farbenfabriken Bayer, Leverkusen), which is very efficient and is soluble in the silicone oils. Another advantage is that there exists a simple method of

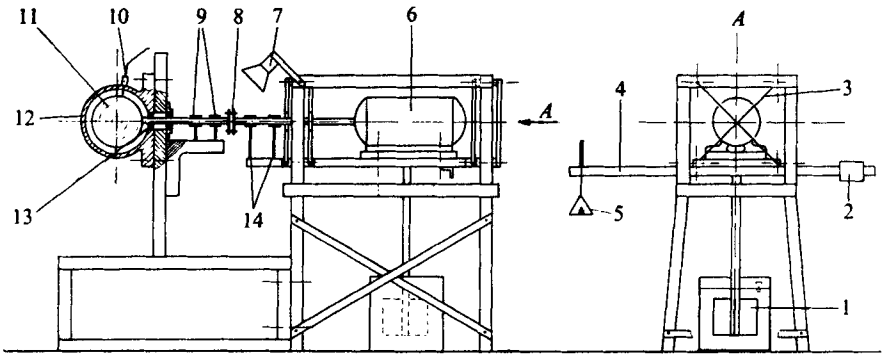

FIGURE 2. Experimental apparatus. (1) Pendulum for damping. (2) Zero adjustment. (3) Spring suspension. (4) Stabilizer. (5) Standard weights for torque measurements. (6) D.c. motor. (7) Stroboscope. (8) Clutch. (9) Roller bearing. (10) Thermocouple. (11) Inner sphere (rotating). (12) Outer sphere (fixed). (13) Sealing ring. (14) Roller bearing.

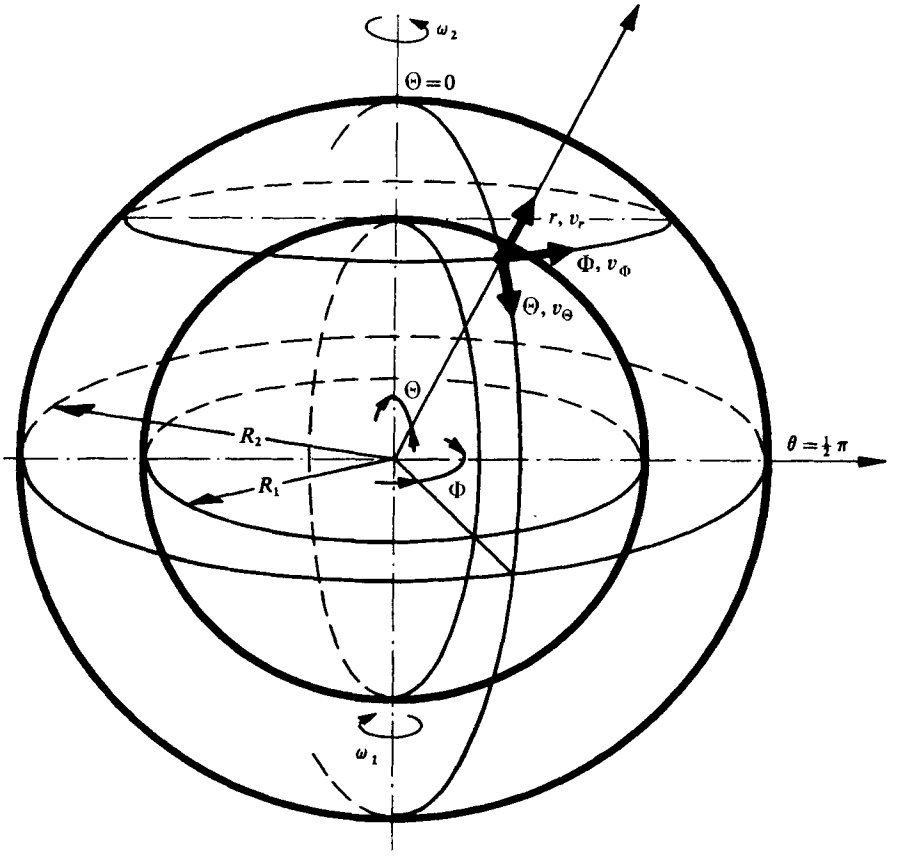

FIGURE 3. Co-ordinates and notation. $v_\Theta = u$, $v_\Phi = v$, $v_r = w$.

discolouring the oil again. By using a certain amount of animal charcoal and then filtering, clear silicone oil can be extracted.

Before particular results are discussed, some remarks on the co-ordinates and notation used should be made. The appropriate co-ordinates are spherical ones. Figure 3 shows the co-ordinates and the corresponding notation for the components of the velocity.

The main parameters influencing the problem are the radius of the inner sphere R_1, the radius of the outer sphere R_2, the width of the gap s, the angular velocities ω_1 and ω_2, the density of the fluid ρ, the dynamic viscosity η (or the kinematic viscosity $\nu = \eta/\rho$), the temperature T and resulting quantities like the moment of rotation M. In order to reduce these parameters, dimensionless characteristic numbers are formed. These are the relative width of the gap $\sigma = (R_2 - R_1)/R_1 = s/R_1$, the Reynolds number $Re = R_1^2\omega_1/\nu$ or the Taylor number $Ta = (R_1 s\omega_1/\nu) \times (s/R_1)^{\frac{1}{2}}$, the ratio of the angular velocities $\mu = \omega_2/\omega_1$ and the friction-torque coefficient $\zeta_M = M/(\frac{1}{2}\rho R_1^5\omega_1^2)$.

3. Flow field between rotating spheres

The type of fluid flow between rotating spheres depends on the Reynolds number and the width of the gap. At very low Re one obtains Stokes flow, whose streamlines are circles around the axis of rotation (see figure 4, plate 1). At higher Re one will get the fully developed three-dimensional basic flow, with streamlines resembling logarithmic spirals (figure 5, plate 1; cf. Sawatzki & Zierep 1970). Close to the inner rotating sphere, the fluid is moving in spirals from the poles to the equator. At the equator, it is deflected outwards and moves back to the poles again in the vicinity of the outer sphere, also in spirals. The spirals join and form a closed flow. Upon increasing Re instabilities appear which will be discussed later.

In order to obtain quantitative data on this flow, measurements were made by the hot-wire technique. For a gap width $s = 6{\cdot}0$ mm, the velocity distribution over the gap was measured in a meridional plane along three radii ($\Theta = 30°$, 50° and 70°). In doing so, the probe was traversed in steps of 0·2 mm. Figure 6 shows the results for several Reynolds numbers for $\Theta = 50°$. The circumferential and meridional velocity are plotted in dimensionless form over the width of the gap. (The radial component of the velocity is very small, except in the neighbourhood of $\Theta = 0$ and 90°, and is not measurable by this method.) The variation of the velocity profiles with Re can be clearly seen. At low Re, the two boundary layers, the inner one at the rotating sphere and the outer one at the stationary sphere, fill the gap. The inner boundary layer is always thinner than the outer one. At higher Re, the boundary layers are separated, and in the middle of the gap a region rotating like a solid body exists (cf. Khlebutin 1968). The meridional velocity approaches zero in this region, which means that the meridional mass transport is transferred into layers near the walls. One thus obtains the typical behaviour of boundary-layer flow. The friction torque for such a flow is independent of the width of the gap, because only the thickness of the core changes, the shape of the boundary layer and the gradient of the circumferential velocity close to the walls, which is responsible for the torque, remaining almost constant.

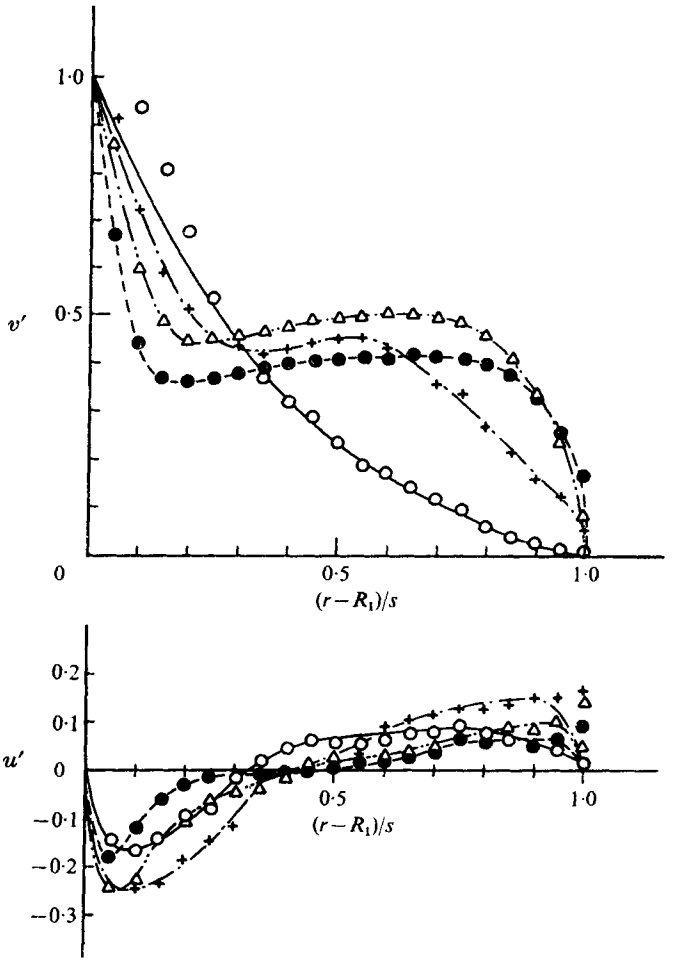

FIGURE 6. Components of the velocity u and v for different Reynolds numbers. $v' = v/R_1 \sin\Theta\omega_1$, $u' = u/R_1 \sin\Theta\omega_1$, $\Theta = 50°$, $R_1 = 74{\cdot}0$ mm, $R_2 = 80{\cdot}0$ mm. -○-, $Re = 4800$; -· × ·-, $Re = 11000$; -· · △ · ·-, $Re = 36750$; - - ● - -, $Re = 73500$.

4. Friction torque

For rotation of the sphere at a constant rate, a rotational moment equal to the frictional torque is needed. This torque was measured for several gap widths and various Reynolds numbers. For all the measurements the temperature gradient was kept close to zero. The friction torque due the roller bearings and sealing rings was measured and controlled after every series of measurements. This was subtracted from the total measured torque to get the net frictional torque of the sphere, and to keep the influence of the friction torque of the bearings a minimum, only total torques larger than ten times the friction torque of the bearings were accepted. By doing so, an accuracy of about 1 % could be achieved.

As a result it is found that the width of the gap is the parameter characterizing the geometry. Yet for all gap sizes investigated there are three distinct flow

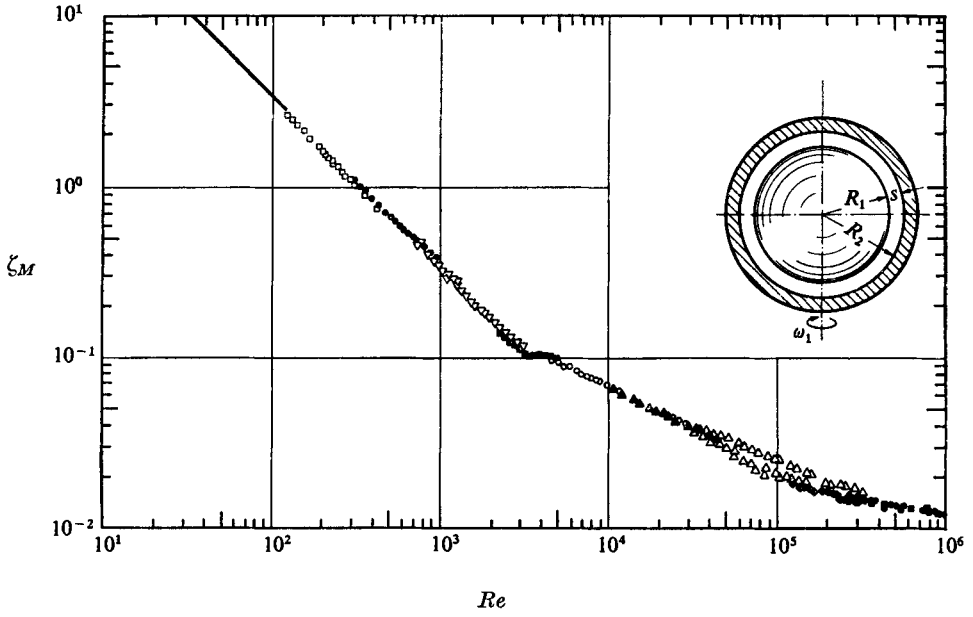

FIGURE 7. Friction torque for $\sigma = 0{\cdot}0527$, $R_1 = 75{\cdot}95$ mm, $R_2 = 79{\cdot}95$ mm, $s = 4{\cdot}0$ mm.

regimes. (This occurs for relatively larger gaps as well and will be discussed after the description of the instabilities.) In a log–log plot of ζ_M *vs.* Re, the measured points lie on stretches of straight lines, so that the three distinct regimes can be clearly observed (figure 7). Sawatzki & Zierep (1970) found that the dimensionless torque for the laminar stable flow satisfied $\zeta_M \sim 1/Re$, for the unstable flow satisfied $\zeta_M \sim 1/Re^{\frac{1}{2}}$ and for the turbulent flow satisfied $\zeta_M \sim 1/Re^{\frac{1}{5}}$. For the laminar stable flow (strictly for Stokes flow only), the torque may be calculated, approximately, with the gap width as a parameter. For very low Re, only the friction terms in the Navier–Stokes equations need be considered, the inertial terms being negligible. By using this approximation Kotschin, Kibel & Rose (1955, p. 353) derived for the circumferential velocity

$$v(r, \Phi) = (c_1 r - c_2/r_2)\sin\Theta,$$

written in spherical co-ordinates, and with the appropriate boundary conditions for the spherical gap,

$$v(r, \Phi) = \frac{\omega_1 R_1^3 \sin\Theta}{r^2(R_2^3 - R_1^3)}(R_2^3 - r^3).$$

The shear stress corresponding to this velocity component is

$$\tau(r, \Phi) = -3\eta\omega_1 R_2^3 \sin\Theta/(R_2^3 - R_1^3)$$

and the moment of rotation is

$$M = 8\pi\eta\omega_1 R_1^3 R_2^3/(R_2^3 - R_1^3).$$

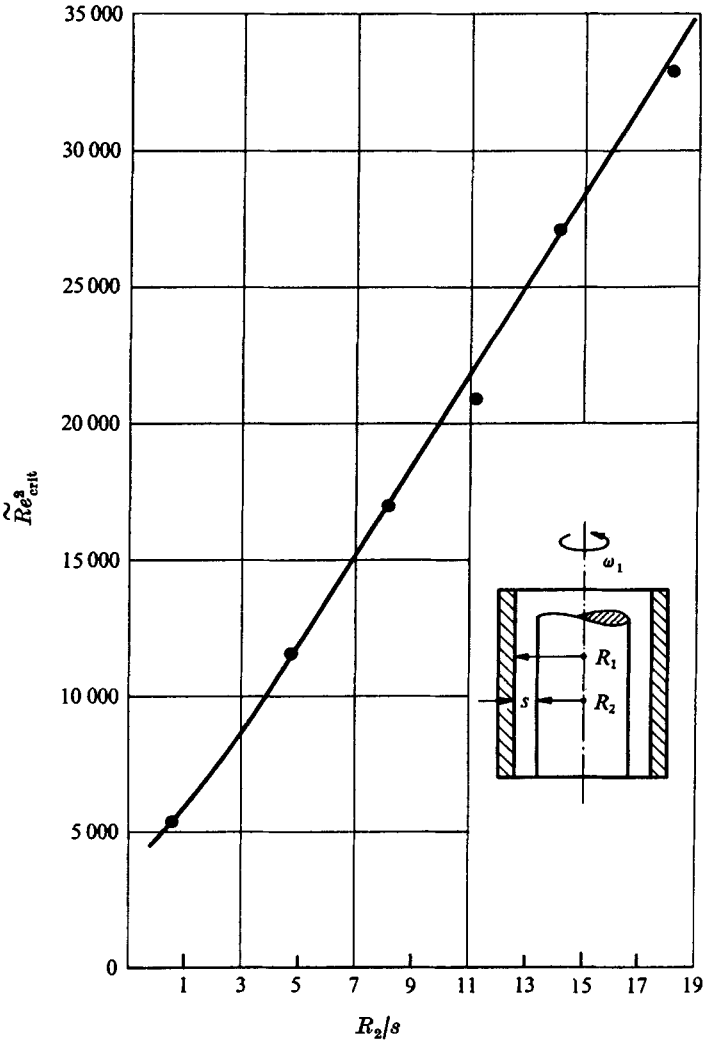

FIGURE 8. Critical Reynolds numbers for arbitrary gap width; $\widetilde{Re} = R_1 s\omega_1/\nu$. ——, theory, Kirchgässner, for cylinders; ●, experiments for spheres.

This is made dimensionless with $\frac{1}{2}\rho/R_1^5\omega_1^2$ to give

$$\zeta_M = \frac{8\pi\eta\omega_1 R_1^3}{\frac{1}{2}\rho R_1^5\omega_1^2}\frac{R_2^3}{(R_2^3-R_1^3)}$$

and finally

$$\zeta_M = \frac{16\pi}{Re}\frac{1}{1-(R_1/R_2)^3}.$$

To get this result the assumption $Re \ll 1$ is made, but surprisingly, for narrow and medium-sized gaps it holds also for higher Re in the whole laminar regime up to the points of transition. For very wide gaps, investigated by Munson & Menguturk (1975), no vortices in the region of transition could be observed. Further-

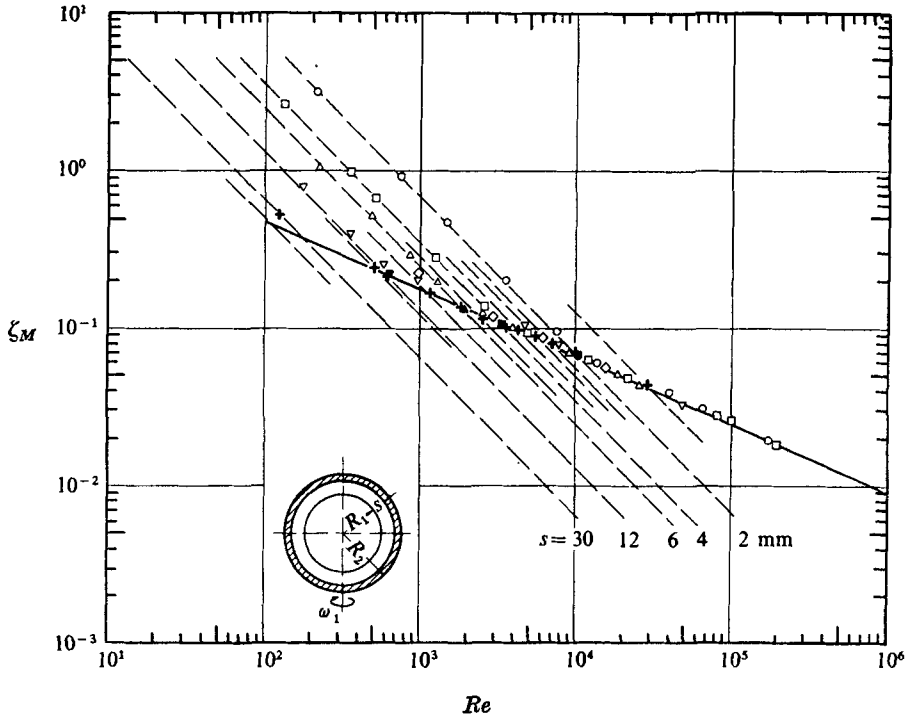

FIGURE 9. Friction torque for arbitrary gap width. Comparison of theory with experiment. – – – –, calculation, $Re \ll 1$. Experiments: ○, s = 2 mm; □, s = 4 mm; △, s = 6 mm; ▽, s = 12 mm; ◇, s = 30 mm. +, points of transition with Kirchgässner's theory for cylinders; ●, ■, ▲, ▼, ◆, experimental points of transition for spheres.

more they found that the torques measured for these gap sizes do not lie on stretches of straight lines up to the transition points, but separate from the straight line at Reynolds numbers lower than the critical value and tend to behave more like results for a free rotating sphere, as shown in figure 10. In the unstable regime, the torque is independent of the width of the gap, hence the measured points for all these gap sizes lie on one straight line. An explanation of this fact is provided by the separation of the inner and outer boundary layer as mentioned above. This means that the points of transition from the laminar stable flow to the unstable flow are the intersections of the calculated straight lines for $Re \ll 1$ and the straight line formed by the results of the experiments for the unstable regime.

On the other hand, the values of the critical Taylor and critical Reynolds number are well known for a cylindrical geometry from Taylor's (1923) theory for small gaps and from Kirchgässner's (1961) theory for arbitrary gap widths. Both theories are derived for rotating cylinders, but the experimental results show that they are valid for the case of rotating spheres too (see figure 8). Using these facts, for all the gap widths investigated a simple method of determining the torque can be given.

Figure 9 explains this method. Using the equation derived above, the torque

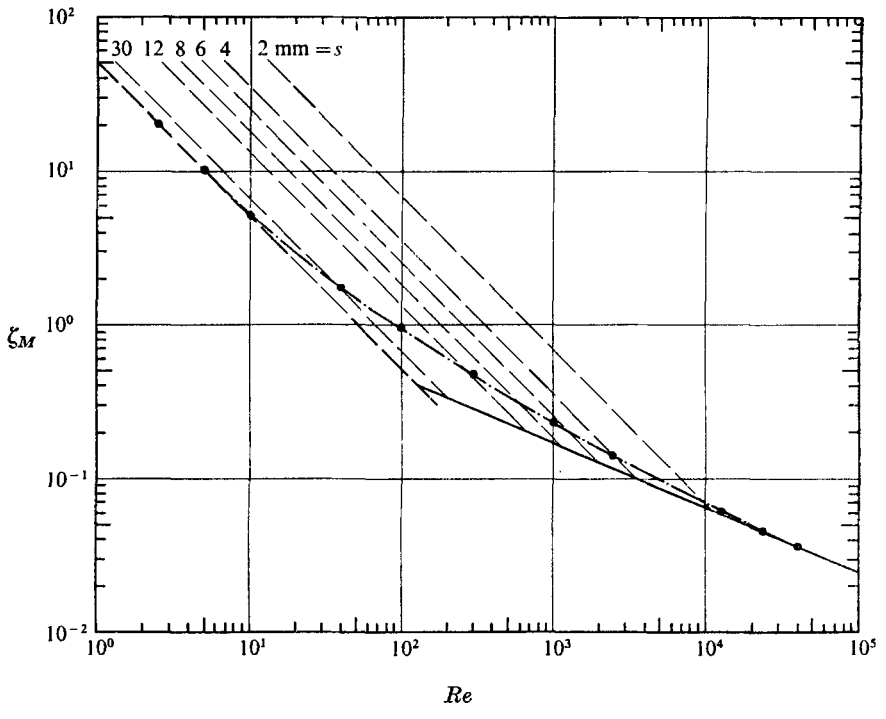

FIGURE 10. Friction torque of a free rotating sphere. – – – –, calculation, $Re \ll 1$, ——, theory for cylinders, Kirchgässner; ●, experiment, Sawatzki.

for laminar stable flow may be calculated for arbitrary gap widths. The next step is to calculate the critical value of the Reynolds number from the theories of Taylor and Kirchgässner. Now, if one marks these Reynolds numbers on the corresponding calculated straight lines, the points of transition in the torque diagram will be obtained. The line through all these points (here marked with a cross) is the straight line on which lie all the measured points for the unstable flow. The agreement between this theoretical method and the experiments is remarkable.

On increasing the gap width by increasing the radius of the outer sphere, i.e. as $R_2 \to \infty$, one obtains a free rotating sphere in an infinite fluid. In this case the straight lines determined theoretically are the asymptotes to the torque of such a sphere (figure 10). This is one limit on this method, the other is the onset of turbulence. The significance of this relatively simple method is as follows: it allows one to obtain the torque for rotating spheres over a wide range of Re for all medium and narrow gaps without the trouble of taking measurements.

5. Instabilities

The basic flow in a spherical gap is three-dimensional and forms spirals. Passing the critical Reynolds number causes disturbances to the basic flow. The immediate neighbourhood of the equator can be regarded approximately as a region

between coaxial cylinders. Therefore, here disturbances are the same as those Taylor observed in the gap between rotating cylinders, namely regular closed vortex cells. Because Görtler (1940) obtained the same vortices for the flow along concave curved walls, we call them Taylor–Görtler vortices.

The first pair of Taylor–Görtler vortices appears at the equator. For the small-gap case, i.e. $\sigma \leqslant 0{\cdot}1$, more vortices are added in the direction towards the pole with increasing angular velocity, but this region is limited to a zone near the equator. The rest of the flow remains undisturbed even if Re is increased almost to the onset of turbulence (figures 11*a–c*, plate 2). Because the Taylor–Görtler vortices are nearly square in cross-section, and because they fill the whole gap, their wavelength λ, i.e. the distance between two vortices, is related to the width of the gap: $\lambda = 2s$. Accordingly, the vortices broaden as the gap broadens, and in the case of a small gap, the wavelength remains constant for all Re (figures 11*a–c*). For medium-sized gaps, i.e. $\sigma \geqslant 0{\cdot}1$, other conditions prevail and will be discussed later, in § 8. If for small gap widths Re is further increased the vortices become wavy (figure 11*d*, plate 2) before the whole flow changes to a turbulent one, but still with a clearly visible structure.

For all gap sizes discribed here, two rules should be stated before the case of a relatively large gap width is discussed: first, the instabilities always develop in the equatorial plane, and second, the broader the gap the smaller the critical Reynolds number.

In the case of a relatively larger gap width, i.e. $\sigma \geqslant 0{\cdot}1$, the behaviour of the vortices is much more complicated. For these large gaps, instabilities appear, if at all, only in the region near the equator. Here, by increasing Re no more vortices are added. But surprisingly one obtains five different modes of flow in the supercritical region, all existing at the same Re. Neither Khlebutin (1968), for $\sigma = 0{\cdot}19$, nor Munson & Menguturk (1975), for $\sigma = 0{\cdot}135$, reported different flow configurations in the unstable regime, but they are clearly detectable and reproducible. These modes, already described in part by Sawatzki & Zierep (1970), will now be discussed briefly.

One mode exists in the supercritical region with two vortices rotating in opposite directions on each side of the equator (figure 12, plate 3). The axes of the vortices are parallel to the equator. In the equatorial plane, the flow is directed outwards, so that to an observer it looks like a source, and because this mode of flow behaves as is expected, it is called the 'normal' one. The rest of the flow remains undisturbed. For further discussions this kind of unstable flow will be called a double vortex or mode IV. By increasing Re, this mode is changed into a different one having only one vortex on each side of the equator.

This mode, the single vortex or mode III, can also be obtained from the laminar basic flow (figure 13, plate 3). Again, the axes of the vortices are parallel to the equator. But the single vortex is rotating in the opposite direction to the double one, so that the flow in the equatorial plane is now directed inwards and to an observer it looks like a sink. At first glance, this behaviour is astonishing. At the equator the centrifugal forces are a maximum and yet the fluid is travelling in the opposite direction. An explanation of this fact can be obtained by considering the undisturbed flow between the vortex and the pole, which induces the rotation of

the vortex and forces it into this direction. The single vortex has the lowest critical Reynolds number, which means that it is the first mode to appear. It is also the most stable one, because it still occurs at very high Reynolds numbers close to the onset of turbulence.

Both of these kinds of supercritical flow, mode IV as well as mode III, are steady ones with the axes of the vortices parallel to the equator. The next two possible modes are unsteady variations of mode IV and mode III. These modes, an oscillating double vortex, named mode V*a*, and an oscillating single vortex, named mode V*b*, are quite similar and appear under similar conditions. Here the axes of the vortices are no longer parallel but inclined to the equator (figures 14*a*, *b*, plate 4) and the vortices penetrate this plane. Since the axes of the vortices now end in the midst of the flow field, single spots of vorticity are hurled off and travel to the poles. The whole process is periodic.

There is another, fifth mode of flow in the regime of supercritical Reynolds numbers. Surprisingly, no vortex and no disturbance at all will appear, though the critical Taylor number, which characterizes the transition from laminar stable to laminar unstable flow has been well exceeded. In the whole range of *Re*, except during the spin-up procedure, no disturbances are visible and the entire flow is quite similar to the laminar basic flow (figure 14*c*, plate 4). On the other hand, this mode is not laminar stable in the common sense because the friction torque for this mode differs from the laminar solution $\zeta_M \sim 1/Re$ and resembles the boundary solution $\zeta_M \sim 1/Re^{\frac{1}{2}}$ for laminar unstable flow. Furthermore, during the generation of this kind of flow, one can see a trace of a vortex in the vicinity of the equator for a very short time. This vortex ring is very quickly carried to the poles by the three-dimensional flow field, but is clearly visible. This mode of flow exists even at very high *Re*, and the character of the flow will not change in the turbulent region up to the limit of the present experiments ($Re \cong 10^6$). This time, disturbances are induced by a spiral vortex around the pole, sometimes called a Stuart vortex, whose arms extend down to the equatorial plane at high *Re* (figure 14*d*, plate 4). The spiral vortex appears only at high angular velocites, and even at very high *Re* in the turbulent regime, the structure of the spiral vortices is very clearly visible. This vortex is steady and can exist together with each of the different modes of instability in the equatorial region. But these spiral vortices are completely different from the vortices of the Taylor–Görtler type in the equatorial region. The pole vortices are all rotating in the same direction and their axes form logarithmic spirals at a constant angle of approximately 12° to the circumferential direction. Since the basic flow also forms spirals, but with another angle, the two types of spiral cross each other and form an angle of about 30°. This system of spiral vortices around the poles of a rotating sphere is comparable to the vortices which appear in the gap between a rotating disk and a stationary housing. Here one obtains exactly the same configuration in the three-dimensional flow and the angles are now about 14° and 30°, respectively (cf. Wimmer 1974).

For the rotating spheres, another interesting flow configuration exists. As mentioned above, the spiral vortex around the pole can appear together with each of the different equatorial instabilities. But, for a certain range of *Re*, the

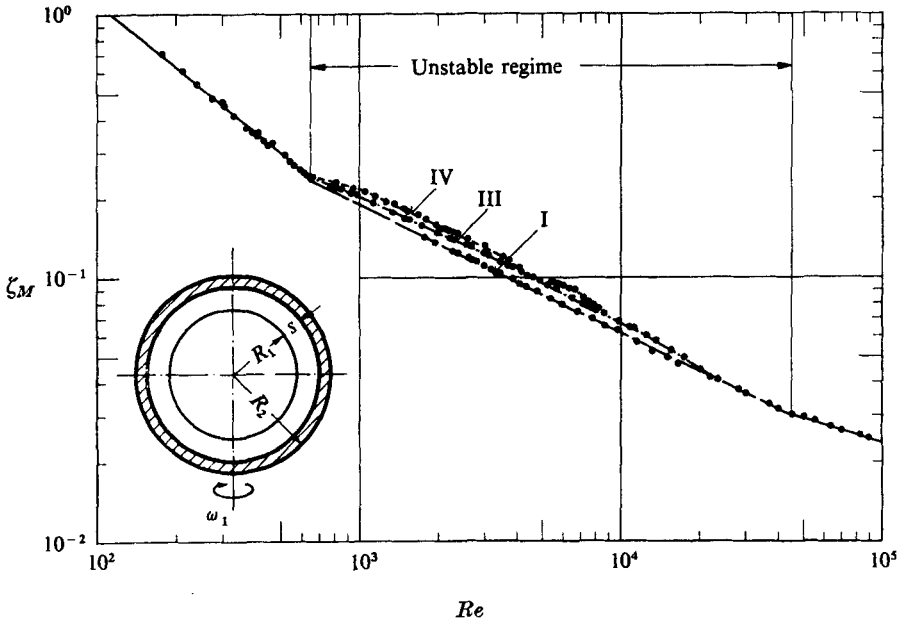

FIGURE 15. Friction torque for relatively large gaps. $\sigma = 0{\cdot}18$, $R_1 = 67{\cdot}80$ mm, $R_2 = 79{\cdot}95$ mm.

two types of instability are separated. That is why instabilities of the Taylor–Görtler type can be obtained at the equator, followed by a region of undisturbed flow and spiral instabilities around the poles, i.e. for rotating spheres a stable flow regime and two different types of instability exist side by side. When the arms of the spirals extend down to the equatorial plane, at higher Re, the two different types of instability overlap and influence each other.

All the instabilities described above are real instabilities, 'stable' ones, say, because vibrations from outside have no influence on the form or the behaviour of the vortices once the vortices are fully developed. It is reasonable that the different modes of flow influence the friction torque. These differences in the friction torque may be measured with clarity. ζ_M for the mode with one vortex is about 2 % less than that for the mode with two vortices on each side of the equator. For supercritical flows with vortices the torque measured is 10 % higher than without vortices (figure 15). Even the spiral vortex around the pole influences the friction torque. Consequently, the torque above $Re = 5500$, at which, for example, the spiral vortex for a 12 mm gap appears, is always higher than the torque one would get for a flow without that spiral vortex. Therefore the characteristic Reynolds numbers describing the transition from one mode of flow to another may also be determined from friction-torque measurements. These transition data are in very good agreement with those obtained by flow visualization.

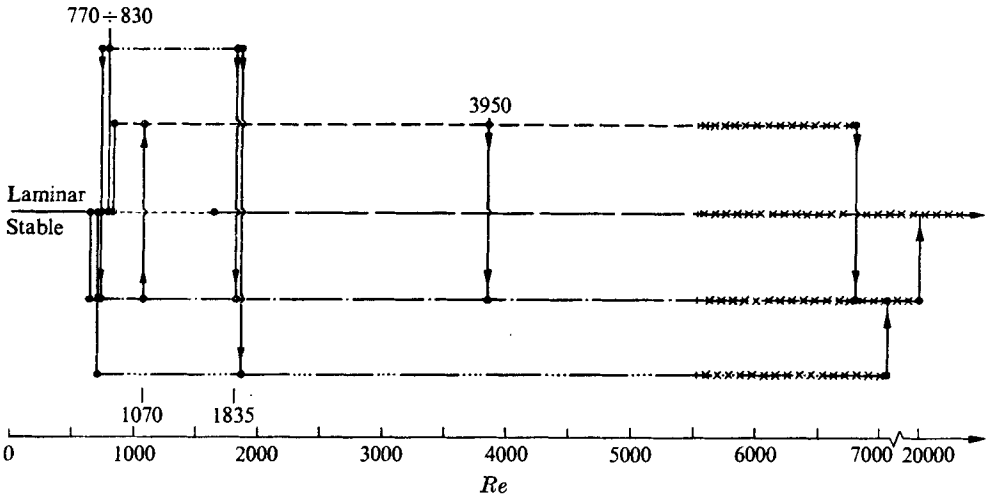

FIGURE 16. Regimes of existence and possibilities of transition for $\sigma = 0{\cdot}18$. – –, mode I; –·–, mode III; ----, mode IV; –···–, mode Va; –·····–, mode Vb; × × × ×, all modes with spiral vortex.

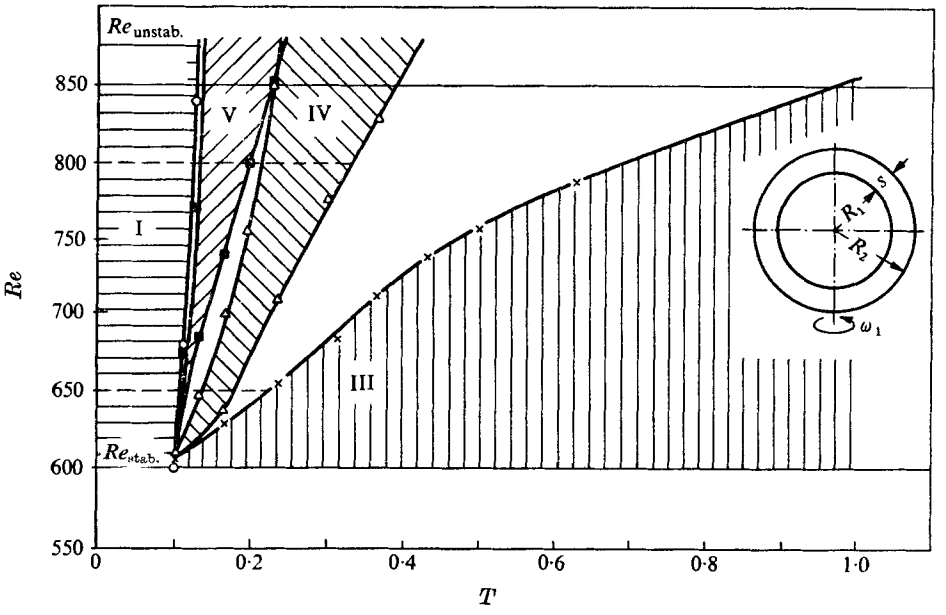

FIGURE 17. Limiting accelerations for the different modes; $T = t\nu/R_{1s}$, $\sigma = 0{\cdot}18$, $d\omega/dt = \dot{\omega} = \ddot{\Phi}$, $\dot{\omega}_{III} = 1{\cdot}5\ s^{-2}$, $2{\cdot}5\ s^{-2} < \dot{\omega}_{IV} < 8\ s^{-2}$, $5\ s^{-2} < \dot{\omega}_{V} < 30\ s^{-2}$, $30\ s^{-2} < \omega_{I}$.

6. Regimes of existence

As mentioned above, all five modes of instability can occur at the same Re but each has a different regime of existence; that is, their first appearance and subsequent disappearance occur at different Re. This behaviour is similar to that described by Coles (1965) for transitions in circular Couette flow. For rotating

spheres the largest regime of existence is observed for the mode without any vortex. It appears last, at a higher Re than all the other modes, but exists up to the boundary of the present experiments at $Re \cong 10^6$. A large regime is also occupied by mode III, one vortex on each side of the equator. This mode is the first of all the modes to appear in the unstable regime and disappears at $Re = 20000$ by changing into mode I after all remaining modes have merged into it. The regimes of existence of the remaining modes are shown in figure 16. The Reynolds numbers given in this figure are only valid for a gap width of $s = 12$ mm, i.e. $\sigma = 0{\cdot}18$. For other gap widths one obtains the same behaviour, but all the data for transition, branching etc. correspond to a smaller Re the broader the gap and vice versa.

Also of great interest, but much more complicated, are the different transitions from one mode to another. Several possibilities of transition are observed for the different modes. As figure 16 shows, mode Va, for example, has three different possible ways of transition into two different other modes, and mode IV has two observed transitions into the same mode. Another interesting thing is that the spiral vortex around the pole always appears at $Re = 5500$, i.e. the first appearance and the existence of this spiral vortex are independent of the different modes of instability in the equatorial region.

7. The generation of the different modes of flow

In the case of relatively larger gap widths the observations of different modes of instability all existing at the same Re is one of the most astonishing phenomena. It is therefore important to know how these different modes of flow are generated. The different modes can be obtained either by a transition from one mode to another or directly from the undisturbed laminar basic flow. Therefore it is obvious that different initial conditions are needed to get these different modes of instability. That is, in the experiment, for each mode a certain acceleration of the inner sphere is needed to get the angular velocity corresponding to the critical Reynolds number. Consequently, the appearance of the different modes of flow depends only on the time needed to reach the Reynolds number for an unstable flow.

The following discussion may explain this fact. Each of the different modes of flow needs a certain amount of energy to develop or to exist, as is shown by the friction-torque measurements, and the transition from the laminar stable to an unstable flow is a transition from one distribution of energy to another. That is, each unstable mode of flow is associated with a certain amount of energy and for the transition a particular time is needed also. By passing through a certain regime very quickly, i.e. with a large acceleration, the viscous fluid flow, owing to its inertia, is unable to follow this fast change and hence the associated mode of flow has no time to develop (cf. mode I). But if the rate of change is slow, i.e. small acceleration, or if there is even a halt at a certain level of energy, the associated mode of flow has sufficient time to develop and to stabilize. Hence, the time-dependent supply of energy, i.e. the rate of change before reaching the supercritical Reynolds number, is responsible for the mode of flow that will appear.

Accordingly, there are different regimes of acceleration for the different modes of flow.

By many measurements, these different regimes of acceleration could be defined and therefore it is possible to predict what kind of flow will appear. Figure 17 shows these experimental results on a plot of Re *vs.* the dimensionless time T ($= t\nu/R_1 s$, where t is the measured time). Because the geometry is kept constant and the viscosity does not change during the short interval of acceleration ($\ll 1\,s$), Re is a measure of the angular velocity. The curves shown in the diagram bound the regions of appearance of a certain mode. Hence all accelerations greater or smaller than those in a particular region generate another mode of flow. In the space between the regions for mode III and mode IV no clearly defined modes of flow are observed. Distinct modes seem not to be able to stabilize, and a transition into mode III or mode IV is observed.

Another result of these measurements is that attention need be paid only to the acceleration in the immediate vicinity of the critical Reynolds number for the generation of a distinct mode of flow. Accelerations outside this small critical region have no influence on the further development. In figure 17, quantitative data for the acceleration $\dot{\omega}$ are given. From these measurements, a prediction of the appearance of each mode is possible. This may give a basis for further theoretical considerations.

The existence of these five different modes of flow at the same Re verifies experimentally the different solution branches of the Navier–Stokes equations in a very clear and impressive way.

8. The dependence of the wavelength on the Reynolds number

Along with these experiments for relatively larger gap widths, there is also a new effect with respect to the wavelength of the vortices. For singly periodic Taylor–Görtler vortices there is no dependence of λ on Re, as for example Burkhalter & Koschmieder (1973, 1974) showed. However, Coles (1965) detected a change in wavelength for a doubly periodic flow. A decrease in the size of vortex cells with increasing Re, as reported by Snyder (1969) and also measured by Burkhalter & Koschmieder (1973), is due to end effects: growth of Ekman cells caused by rotating end plates of the cylinder, which results in a decrease in size of the cells in between. These end effects can not occur for the flow between concentric rotating spheres. For all wavelength measurements in a cylindrical gap only a decrease with Re was observed and Burkhalter & Koschmieder (1973) deduce that this would not be possible if the cylinders were infinite.

Thus, for all experiments with cylinders (provided that the initial conditions are comparable), the wavelength for singly periodic vortices remains constant for constant gap width for all Re. This rule does not hold for the vortices in a relatively larger spherical gap. As may be expected, the wavelength is different for the different modes of instability at the same Re, but that the wavelength of a single mode (same initial conditions) is variable is a novelty. Here, for the first time for singly periodic Taylor–Görtler instabilities, the wavelength of the vortices is no longer independent of Re. As figure 18 shows, this effect is quite

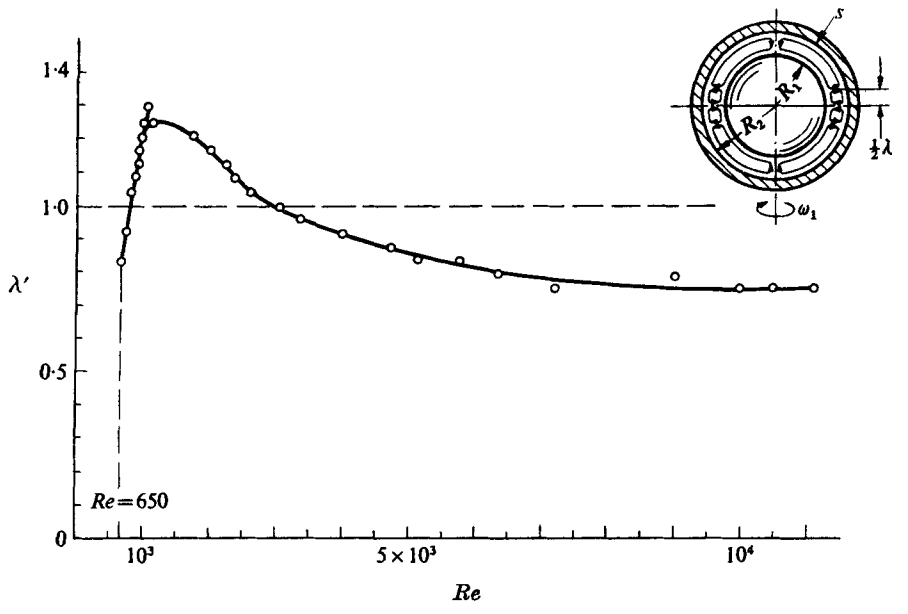

FIGURE 18. Wavelength as function of Re for mode III. $\sigma = 0{\cdot}18, \lambda' = \lambda/2\,s$.

pronounced. These measurements have been made for the case of a single vortex on each side of the equator. The dimensionless half-wavelength $\lambda' = \lambda/2s$† is plotted *vs.* Re. At $\lambda' = 1$, the latitudinal extent of the vortex is equal to the width of the gap. Therefore it is easy to see that the width of the vortex can be smaller or greater than the gap width. Initially, the vortex is relatively small, but when Re is increased it grows quickly, reaches its maximum, becomes smaller again, and finally remains nearly constant. Consequently, large wavelengths are obtained only at low to medium Re. This effect is subject to the rest of the three-dimensional flow, which compresses the vortex more or less depending on the angular velocity. In this way, variations in wavelength of more than 100 % have been observed (figure 19).

Figure 19 shows the development of the wavelength in the case of a transition from one mode of flow to another. If in the lower range of Re the angular velocity is changed very carefully and slowly, the course of the wavelength curve is also changed. With increasing Re the width of the vortex finally reaches a value which is above the maximum of the steady curve. Exactly at this point of greatest wavelength ($\lambda' = 1{\cdot}3$), located at $Re = 1060$, the single-vortex mode (mode III) changes into the mode with two vortices on each side of the equator (mode IV). Simultaneously, the width of the vortex near the equator is reduced to $\lambda' = 1{\cdot}05$. But on increasing Re the wavelength again increases and then diminishes after reaching a maximum at $\lambda' = 1{\cdot}2$. The smallest value of the width of the vortex near the equator is measured with $\lambda' = 0{\cdot}54$ for $Re = 3950$, i.e. the Re of the

† By definition, the wavelength λ equals the width of a double vortex, but in the diagrams, only $\frac{1}{2}\lambda$ is used, because this quantity can be measured with a high degree of accuracy.

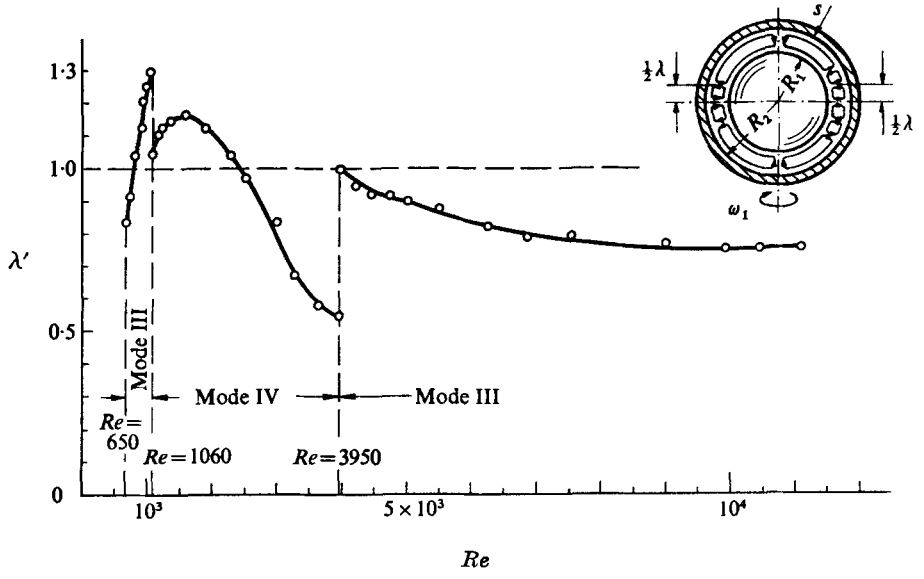

FIGURE 19. Development of the wavelength for transition from mode III to mode IV. $\sigma = 0{\cdot}18, \lambda' = \lambda/2$ s.

transition from mode IV to mode III. At this point, the width of the vortex suddenly jumps to the significantly higher value of the width of the gap. The further development is similar to that described in figure 18 for mode III, i.e. the wavelength tends asymptotically to a constant value.

The diagrams apply only to the development of the vortex near the equator, the more distant vortex of mode IV remaining almost unchanged with $\lambda' = 0{\cdot}9$.

The phenomenon of the different wavelengths for different Re, which was observed here for the first time, has been investigated not only qualitatively, but also quantitatively. It can be explained only by an interchange of the secondary flow and the three-dimensional basic flow. The sudden change in the wavelength happens exactly at those Re at which the transition from one mode to another takes place. So a third, independent method of determining the transitions, besides flow visualization and friction-torque measurements, is available which gives exactly the same data. Precisely at these sudden transitions, i.e. at the points of maximum or minimum width of the vortices, the vortices become either too large ($\lambda' = 1{\cdot}3$) or too small ($\lambda' = 0{\cdot}54$) to be stable. This change in the wavelength and the resulting deformation is probably the reason for the transition from one mode to another, because the vortices always jump back to a width equal to the width of the gap.

The research reported in this paper has been supported by the Deutsche Forschungsgemeinschaft (DFG).

REFERENCES

BRAILOVSKAYA, I. YU., ASTAFEVA, N. M. & YAVORSKAYA, I. M. 1972 Nonstationary compressible viscous fluid motion in a spherical layer. *Fluid Dyn.* **7**, 370.

BRATUKHIN, YU. K. 1961 An estimate of critical Reynolds number for fluid flow between two rotating spherical surfaces. *J. Appl. Math. Mech.* **25**, 1286.

BURKHALTER, J. E. & KOSCHMIEDER, E. L. 1973 Steady supercritical Taylor vortex flow. *J. Fluid Mech.* **58**, 547.

BURKHALTER, J. E. & KOSCHMIEDER, E. L. 1974 Steady supercritical Taylor vortices after sudden starts. *Phys. Fluids*, **17**, 1929.

COLES, D. 1965 Transition in circular Couette flow. *J. Fluid Mech.* **21**, 385.

DONNELLY, R. J. 1965 Experiments on the stability of viscous flow between rotating cylinders. *Proc. Roy. Soc.* A**283**, 509.

GÖRTLER, H. 1940 Über seine dreidimensionale Instabilität laminarer Grenzschichten an konkaven Wänden. *Nachr. Ges. Wiss. Göttingen Math. Phys. Kl. Neue Folge I*, vol. 2, 1.

KHLEBUTIN, G. N. 1968 Stability of fluid motion between a rotating and stationary concentric sphere. *Fluid Dyn.* **3** (6), 31.

KIRCHGÄSSNER, K. 1961 Die Stabilität der Strömung zwischen zwei rotierenden Zylindern gegenüber Taylor-Wirbeln für beliebige Spaltweiten. *Z. angew.Math. Phys.* **12**, 14.

KOTSCHIN, N. J., KIBEL, I. A. & ROSE, N. W. 1955 *Theoretische Hydrodynamik*, vol. 2. Berlin: Akademie-Verlag.

MUNSON, B. R. & JOSEPH, D. D. 1971 Viscous incompressible flow between concentric rotating spheres. Parts 1 and 2. *J. Fluid Mech.* **49**, 289.

MUNSON, B. R. & MENGUTURK, M. 1975 Viscous incompressible flow between concentric rotating spheres. Part 3. *J. Fluid Mech.* **69**, 705.

OVSEENKO, J. G. 1963 Über die Bewegung einer viskosen Flüssigkeit zwischen zwei rotierenden Kugelflächen *Isv. VUZ, Math.* **4**, 129.

RITTER, C. F. 1973 Berechnung der zähen, inkompressiblen Strömung im Spalt zwischen zwei konzentrischen rotierenden Kugelflächen. Dissertation, Universität (TH) Karlsruhe.

SAWATZKI, O. 1970 Das Strömungsfeld um eine rotierende Kugel. *Acta Mechanica*, **9**, 159.

SAWATZKI, O. & ZIEREP, J. 1970 Das Stromfeld im Spalt zwischen zwei konzentrischen Kugelflächen, von denen die innere rotiert. *Acta Mechanica*, **9**, 13.

SNYDER, M. A. 1969 Wave-number selection at finite amplitude in rotating Couette flow. *J. Fluid Mech.* **35**, 273.

TAYLOR, G. J. 1923 Stability of a viscous liquid contained between two rotating cylinders. *Phil. Trans.* A **223**, 289.

WIMMER, M. 1974 Experimentelle Untersuchungen der Strömung im Spalt zwischen zwei konzentrischen Kugeln, die beide um einen gemeinsamen Durchmesser rotieren. Dissertation, Universität (TH) Karlsruhe.

YAKUSHIN, V. J. 1968*a* Steady motion of a viscous fluid in a spherical layer. *Fluid Dyn.* **3** (2), 94.

YAKUSHIN, V. J. 1968*b* Motion of a fluid between two rotating concentric spheres. *Fluid Dyn.* **3** (6), 35.

YAKUSHIN, V. J. 1969 Stability of fluid motion in a thin spherical layer. *Fluid Dyn.* **4** (1), 83.

YAKUSHIN, V. J. 1970 Stability of the motion of a liquid between two rotating concentric spheres. *Fluid Dyn.* **5**, 660.

ZIEREP, J. & SAWATZKI, O. 1970 Three-dimensional instabilities and vortices between two rotating spheres. 8th *Symp. Naval Hydrodyn.* (cf. Sawatzki & Zierep, 1970).

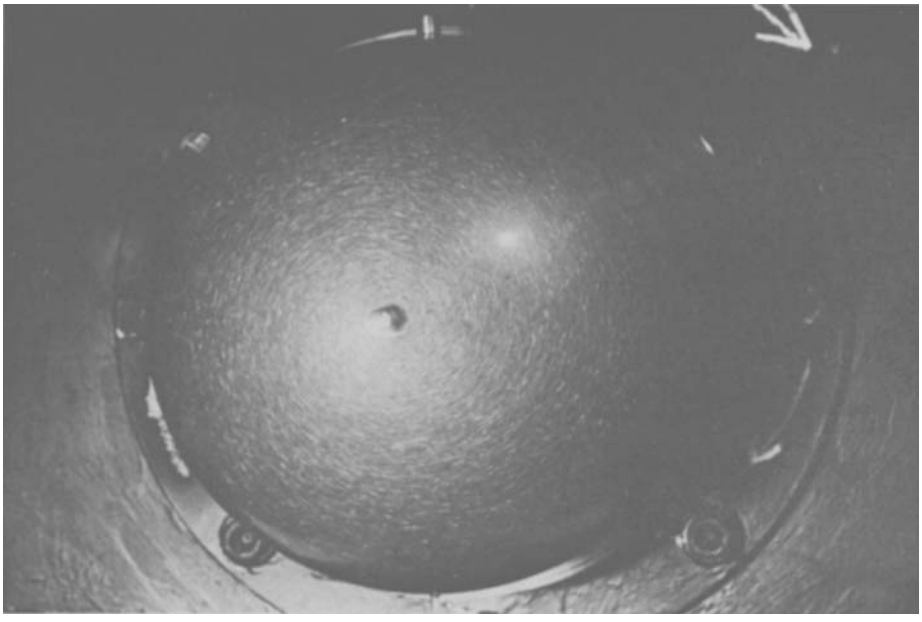

FIGURE 4. Concentric circles for the Stokes flow. $\sigma = 0{\cdot}066$, $R_1 = 75{\cdot}0$ mm, $R_2 = 80{\cdot}0$ mm, $Re = 10$.

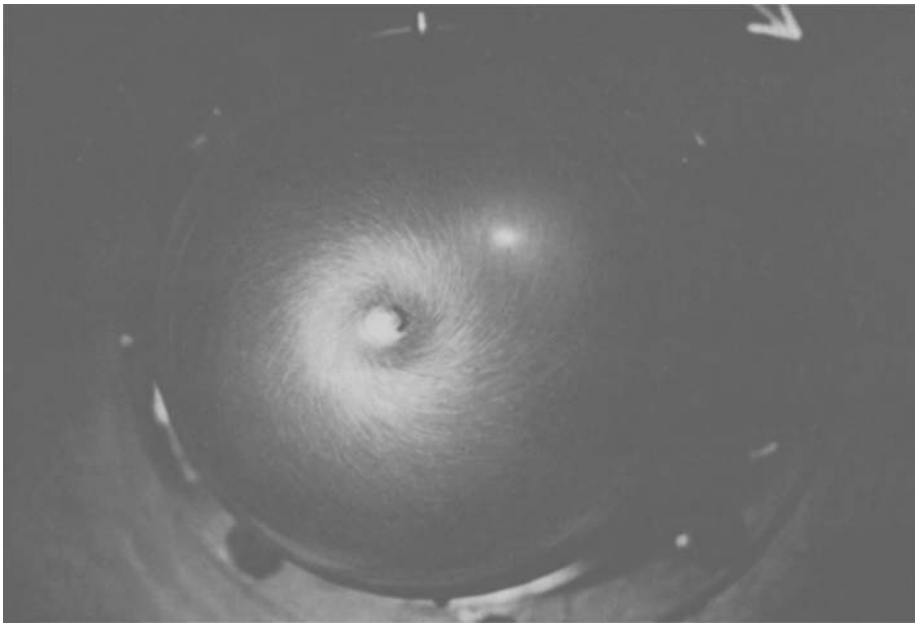

FIGURE 5. Spirals for the three-dimensional flow. $\sigma = 0{\cdot}066$, $R_1 = 75{\cdot}0$ mm, $R_2 = 80{\cdot}0$ mm, $Re = 2250$.

(*Facing p.* 336)

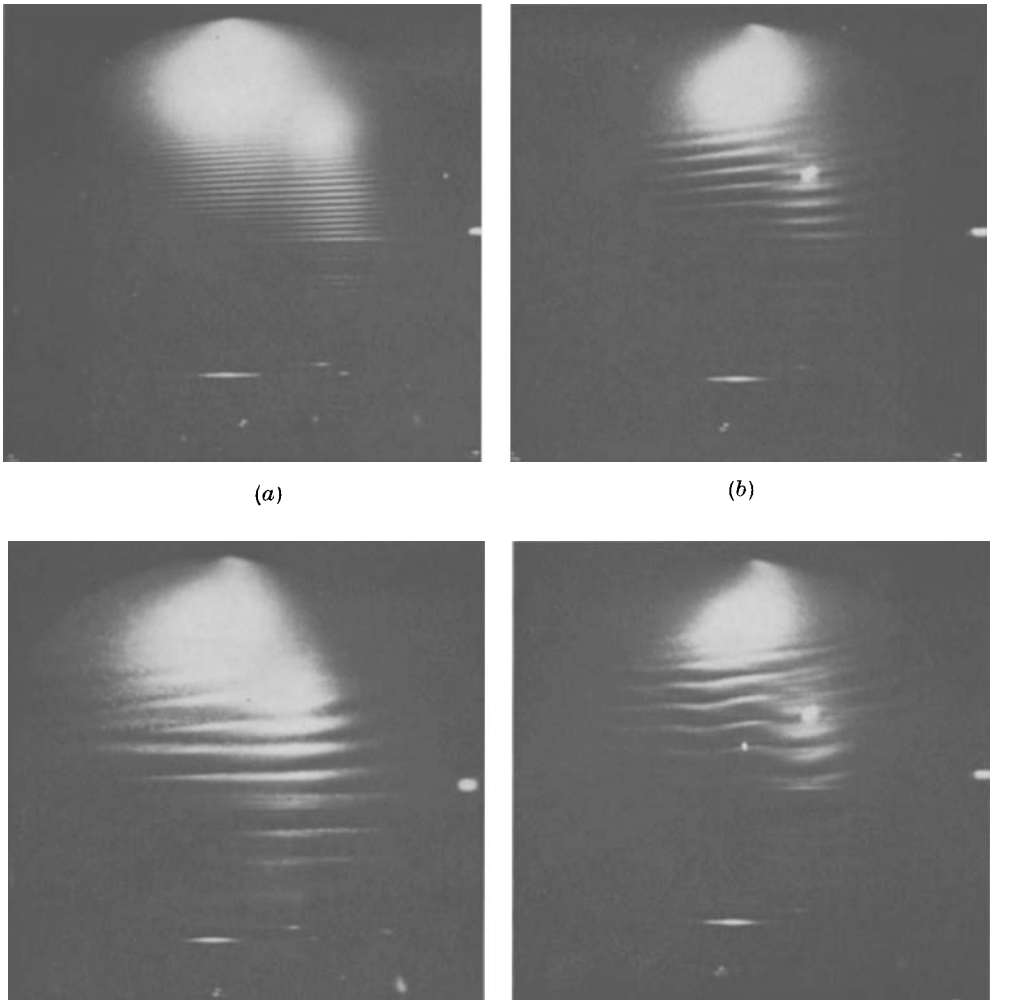

(*a*) (*b*)

(*c*) (*d*)

FIGURE 11. Taylor–Görtler vortices. $R_2 = 80{\cdot}0$ mm. (*a*) $\sigma = 0{\cdot}0133$, $R_1 = 78{\cdot}95$ mm, $Re = 27\,000$, $Ta = 41{\cdot}6$. (*b*) $\sigma = 0{\cdot}046$, $R_1 = 76{\cdot}5$ mm, $Re = 7900$, $Ta = 77{\cdot}3$. (*c*) $\sigma = 0{\cdot}066$, $R_1 = 75{\cdot}0$ mm, $Re = 7100$, $Ta = 122$. (*d*) The axes of the vortices become wavy; $\sigma = 0{\cdot}046$, $R_1 = 76{\cdot}5$ mm, $Re = 10\,400$, $Ta = 101$.

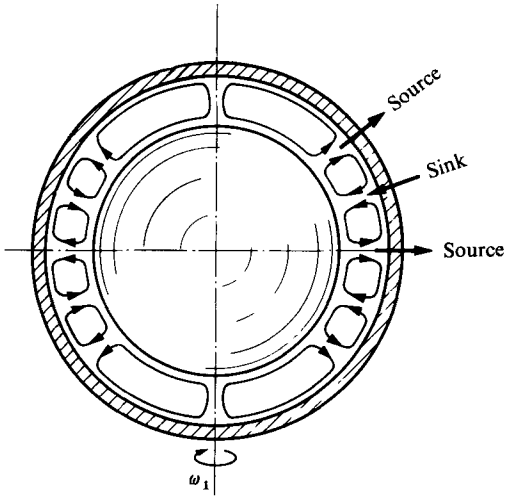

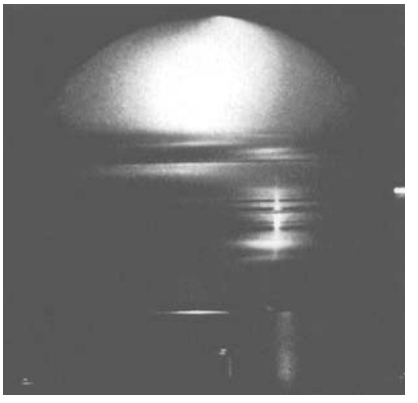

FIGURE 12. Sketch and photograph of mode IV; $\sigma = 0{\cdot}18$, $R_1 = 67{\cdot}80$ mm, $R_2 = 79{\cdot}95$ mm.

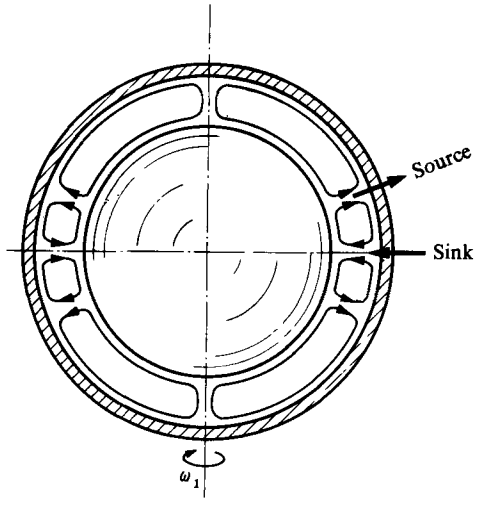

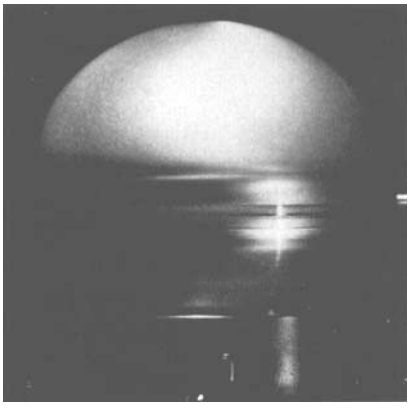

FIGURE 13. Sketch and photograph of mode III; $\sigma = 0{\cdot}18$, $R_1 = 67{\cdot}80$ mm, $R_2 = 79{\cdot}95$ mm.

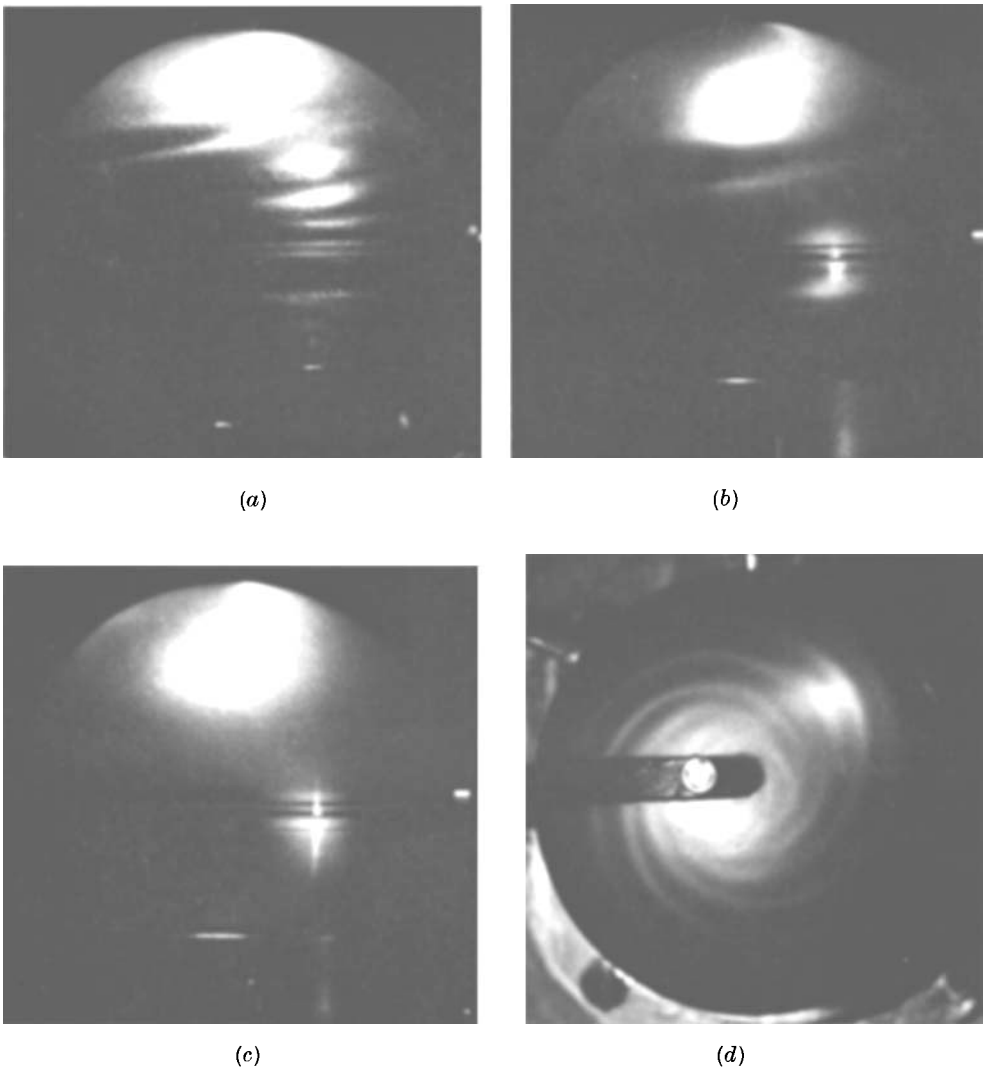

(*a*) (*b*)

(*c*) (*d*)

FIGURE 14. (*a*) Mode V*a*: oscillating double vortex. (*b*) Mode V*b*: oscillating single vortex. (*c*) Mode I: supercritical flow without disturbances. (*d*) Spiral vortex around the pole. $\sigma = 0{\cdot}18$, $R_1 = 67{\cdot}80$ mm, $R_2 = 79{\cdot}95$ mm.